MetaTap: Resonance-Splitting-Based Multi-Dip Encoding for High-Resolution Water Contaminant Sensing

JUEXING WANG, Michigan State University, United States
BINBIN XIE, University of Texas at Arlington, United States
MINHAO CUI, Seoul National University, Republic of Korea
YIMENG LIU, Michigan State University, United States
XIAO ZHANG, University of Michigan-Dearborn, United States
RUOFENG LIU, Michigan State University, United States
HUACHENG ZENG, Michigan State University, United States
ZHICHAO CAO, Michigan State University, United States
JIE XIONG, Nanyang Technological University, Singapore
TIANXING LI*, Michigan State University, United States

Ensuring drinking water safety is critical, yet detecting ppb-level heavy metals remains a challenge, as health-relevant regulatory thresholds (e.g., 10 ppb) are three to seven orders of magnitude below the sensitivity of currently available test strips and wireless sensing systems. This paper presents MetaTap, a low-cost, passive metasurface-based system for high-resolution water contamination detection. Inspired by resonance splitting, MetaTap employs a novel Complementary Asymmetric Split Square (CASS) structure that encodes multiple information-rich resonance dips within the bandwidth of a commercial UWB radar. This design significantly enhances sensing resolution, enabling the detection of contaminants at concentrations as low as 5 ppb. To ensure robustness in complex environments, we develop a physically interpretable model using resonance spectral features and their derivatives to suppress noise from multipath propagation and unknown background constituents. Extensive evaluations in real-world scenarios demonstrate that MetaTap maintains strong robustness against environmental variations and achieves an average detection accuracy of 94.6% for contaminants in real tap water. With a metasurface fabrication cost of only $0.10, MetaTap provides a highly accessible and sensitive platform for real-time water quality monitoring in everyday settings.

CCS Concepts: • **Human-centered computing → Ubiquitous and mobile computing systems and tools**.

Additional Key Words and Phrases: Metasurface design; Low-cost sensing; Physically interpretable model; UWB sensing

ACM Reference Format:
Juexing Wang, Binbin Xie, Minhao Cui, Yimeng Liu, Xiao Zhang, Ruofeng Liu, Huacheng Zeng, Zhichao Cao, Jie Xiong, and Tianxing Li. 2026. MetaTap: Resonance-Splitting-Based Multi-Dip Encoding for High-Resolution Water Contaminant

*Corresponding author.

Authors' Contact Information: Juexing Wang, Michigan State University, United States, wangjuex@msu.edu; Binbin Xie, University of Texas at Arlington, United States, binbin.xie@uta.edu; Minhao Cui, Seoul National University, Republic of Korea, minhaocui@snu.ac.kr; Yimeng Liu, Michigan State University, United States, liuyime2@msu.edu; Xiao Zhang, University of Michigan-Dearborn, United States, zhanxiao@umich.edu; Ruofeng Liu, Michigan State University, United States, liuruofe@msu.edu; Huacheng Zeng, Michigan State University, United States, hzeng@msu.edu; Zhichao Cao, Michigan State University, United States, caozcthu@gmail.com; Jie Xiong, Nanyang Technological University, Singapore, jie.xiong@ntu.edu.sg; Tianxing Li (corresponding author) Michigan State University, United States, litianx2@msu.edu.

This work is licensed under a Creative Commons Attribution 4.0 International License.
© 2026 Copyright held by the owner/author(s).
ACM 2474-9567/2026/6-ART62
https://doi.org/10.1145/3810188

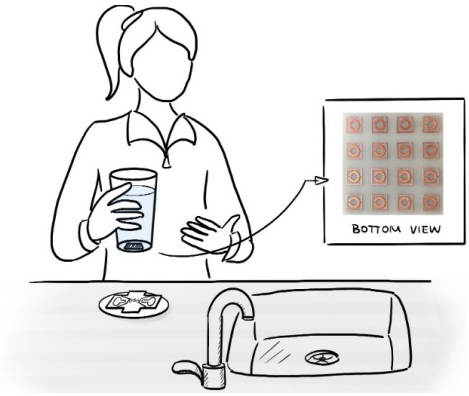

Fig. 1. Illustration of MetaTap operation in daily use. Tap water is placed in a cup embedded with a passive metasurface. When positioned above a UWB radar, the metasurface modulates the reflected signals based on the water's dielectric properties. The processed reflections are used to estimate heavy-metal contamination levels in real time.

Sensing. *Proc. ACM Interact. Mob. Wearable Ubiquitous Technol.* 10, 2, Article 62 (June 2026), 27 pages. https://doi.org/10.1145/3810188

1 INTRODUCTION

Accessing safe drinking water remains a persistent global challenge, affecting over 2.1 billion people worldwide [28]. Drinking water contamination typically stems from industrial discharge, aging infrastructure, and agricultural runoff. Exposure to heavy metal contaminants in tap water poses serious health risks even at low concentrations, as evidenced by the Flint water crisis [36, 41] and contamination in Brazil's Xikrin do Cateté territory [8]. Such contamination has been associated with adverse health outcomes, including kidney dysfunction, developmental delays, and impaired fetal growth [2, 18]. However, hazardous substances in drinking water are often odorless and colorless, making them imperceptible without specialized tools. Laboratory-grade instruments provide precise chemical analysis but are often cost-prohibitive, with prices exceeding $20,000 [5]. In contrast, common test strips, while accessible for household use, offer only coarse detection granularity (e.g., ~50 ppm). This sensitivity is more than three orders of magnitude lower than health-relevant regulatory thresholds [36, 46].

Emerging wireless liquid sensing systems have gained significant traction for identifying and classifying everyday liquids. Fig. 2 provides an overview of the diverse techniques developed for wireless water quality monitoring. These approaches can be broadly categorized into three classes: (i) RF direct sensing [17, 22, 29, 43–45], which exploits correlations between RF signal propagation and bulk liquid properties; (ii) tag-based sensing [20, 52, 53], where RFID or resonant tags are attached to containers to infer changes in liquid composition; and (iii) metasurface-based sensing [10], which leverages passive metastructures to enhance signal-liquid interactions. Compared to high-cost laboratory instruments and low-sensitivity chemical test strips, these wireless systems provide a compelling balance between accessibility and performance, making them ideal for ubiquitous water quality screening.

However, due to their limited sensitivity, existing wireless liquid sensing systems are primarily tailored for coarse-grained liquid classification. Traditional systems typically operate at the percentage level (~1%, or 10^7 ppb), while even state-of-the-art work [10] only achieves tens of parts-per-million (ppm). These benchmarks remain three to seven orders of magnitude above the part-per-billion (ppb) sensitivity required to detect hazardous, imperceptible contaminants, falling far short of regulatory requirements. To bridge this substantial resolution

gap, there is an urgent need for novel, low-cost, mobile sensing platforms that are capable of detecting ppb-level contamination. Such platforms would enable early detection of odorless and colorless contaminants that currently elude both human perception and conventional consumer-grade test strips [14, 50]. However, contaminant-induced signal perturbations at the ppb level are extremely subtle and often obscured by multiple factors, including interference from co-existing components in water, background noise, and multipath effects.

This leads to an important research question: *Can wireless sensing resolution be significantly enhanced to enable robust and high-precision water contamination detection in complex, real-world daily scenarios?* Our key idea is inspired by the *resonance splitting* effect achieved through a novel metasurface design. The resonance splitting effect refers to the division of a single resonance notch into two or more distinct dips. This effect is induced by structural asymmetry or coupling interactions that modify the system's energy distribution, break its original equilibrium, and lead to the emergence of multiple resonant modes [13, 47, 54]. By transforming the conventional symmetric complementary split-ring (CSR) structure into an asymmetric resonance-split configuration, our metasurface design effectively induces the resonance splitting effect, yielding two key advantages:

- Enhanced Signal Responsiveness. The resonance dips function as "magnifiers" that significantly amplify the subtle signal perturbations induced by ultra-low concentration levels of liquid contaminants. By selectively leveraging these high-sensitivity regions, our design improves the signal-to-noise ratio (SNR), thereby pushing the sensing resolution toward the ppb level, a regime previously considered inaccessible to conventional wireless approaches.
- Multi-Dimensional Feature Encoding. Beyond simple amplification, the resonance splitting effect introduces multiple information-rich dips that serve as diverse feature channels. This increased spectral dimensionality enables the system to distinguish target contaminants from co-existing materials while effectively suppressing background noise. By providing multiple correlated responses, this multi-dip configuration enhances reliability and robustness in uncontrolled environments.

Combined, these two mechanisms create a synergistic effect: the amplified responsiveness lowers the detection boundary for wireless signals, while the enhanced robustness stabilizes the measurement against interference. Together, they bridge the three orders of magnitude gap, enabling reliable wireless sensing at the ppb-level concentrations.

With the proposed metasurface design, we present MetaTap, a low-cost, high-resolution drinking water contamination detection system for everyday use. As shown in Fig. 1, users can assess water contamination levels by simply placing tap water in a cup embedded with a passive metasurface and positioning it above an ultra-wideband (UWB) radar. The radar transmits signals that interact with the metasurface, encoding liquid-specific information into the modulated reflection. These reflected signals are then captured and processed to extract the unique electromagnetic signatures corresponding to distinct heavy metal concentrations. Compared to prior works categorized in Fig. 2, MetaTap achieves a sensing resolution of 5 ppb, enabling reliable ppb-level detection. Such resolution enables routine, direct screening of imperceptible heavy metals in accordance with regulatory thresholds, a capability previously unattainable for wireless sensing systems. Beyond sensitivity, however, the transition from a laboratory prototype to a practical system requires a careful balance between cost, portability, and environmental robustness. MetaTap is specifically designed to reconcile these competing requirements within a unified architecture. Several remaining technical challenges must be addressed to enable full field deployment.

First, establishing an interpretable model that captures the complex mapping between reflected signal and contaminant concentrations remains a significant challenge. Previous wireless sensing systems primarily rely on machine learning [10, 20, 22] to approximate these relationships. Although successful in controlled settings, such black-box approaches frequently lack the interpretability and generalizability required for varied real-world environments. To address these limitations, we developed a comprehensive analytical model that characterizes the relationship between the amplitude–phase response and contaminant concentration. This formulation provides

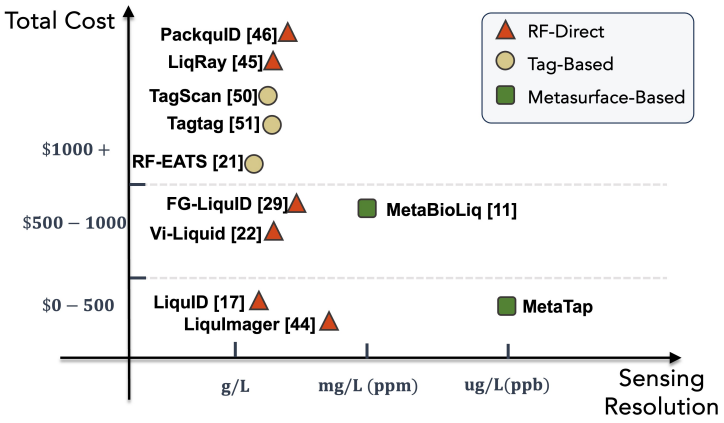

Fig. 2. Wireless liquid sensing approaches: RF-Direct, Tag-Based (RFID Tags), and Metasurface-Based.

a rigorous theoretical foundation for the system and offers insights into the underlying sensing mechanism, enabling more robust predictions across varying scenarios.

Second, ensuring system robustness and adaptability across diverse real-world environments is a critical challenge. Household settings introduce complex multipath effects that complicate signal propagation. To mitigate these interferences, we analyze the phase and amplitude derivatives of the reflected signal, enabling the system to decorrelate metasurface reflections from environmental interference. Furthermore, we employ a feature-alignment strategy to synchronize spectral transitions across different modalities, ensuring that information-rich bands are consistently identified regardless of localized spectral shifts. By overcoming these environmental and signal-level instabilities, MetaTap ensures consistent performance, enabling accessible water quality screening in everyday scenarios

The overall system cost of MetaTap remains highly competitive. The UWB radar module, priced at approximately $150, is significantly cheaper than previous mmWave radar systems (~$800) [10]. Furthermore, the passive metasurface tag is manufactured at a cost of only $0.10. Although the metasurface is designed as a low-cost and replaceable component, it is sufficiently durable to be reused for several months with routine cleaning, offering a cost-effective and sustainable alternative to chemical test strips. The main contributions of MetaTap are summarized as follows:

- To the best of our knowledge, MetaTap is the first wireless sensing system to leverage the resonance splitting effect to encode richer information and increase the signal SNR through a novel metasurface design, achieving a three orders of magnitude improvement in wireless liquid sensing resolution.
- We propose a mathematical model that captures the relationship between signal characteristics and contaminant concentration, establishing a theoretical foundation for interpretable and fine-grained water contaminant monitoring.
- By exploiting the derivatives of phase and amplitude features and extracting informative points, we effectively mitigate multipath interference and enhance system robustness in challenging real-world environments.
- With the proposed $0.10 metasurface and a sub-$150 portable radar system, MetaTap offers an affordable and scalable solution for large-scale water quality monitoring, achieving ppb (μg/L)-level resolution and 94.6% prediction accuracy across common tap water contaminants and benign substances.

(a) Basic Design (b) Equivalent Circuit

Fig. 3. Surface layer structure and equivalent circuit of the basic metasurface unit.

2 BACKGROUND

The basic principle of RF liquid sensing is that liquids with different compositions exhibit different dielectric permittivity, which affects the reflected RF signals. Based on the Debye Equation [32] and the Cole–Cole model [12, 38], the permittivity $\hat{\epsilon_l}$ of liquid as a function of the reflected signal frequency ω can be expressed as

$$\hat{\epsilon_l}(\omega) = \epsilon_\infty + \frac{\epsilon_s - \epsilon_\infty}{(1 + j\omega\tau)^{(1-\alpha)}}, \tag{1}$$

where ϵ_s represents the static permittivity at the low-frequency limit; ϵ_∞ is the permittivity at the high-frequency limit; τ denotes the characteristic dielectric relaxation time; and α is the distribution parameter accounting for the relaxation-time spread. In addition to the intrinsic permittivity of the solvent, the overall permittivity of a liquid solution is influenced by the solute concentration. For a dilute solution under constant temperature and operating frequency ω, its effective permittivity can be expressed as [25]

$$\epsilon_l(\omega) = \epsilon_u(\omega)(1 - \phi) + \epsilon_t(\omega)\phi, \tag{2}$$

where ϵ_u is the permittivity of solvent and ϵ_t corresponds to the solute permittivity at frequency ω. Additionally, ϕ denotes the mole fraction of solvents or concentration level in the mixture. Different concentration levels of the target element modify the effective permittivity of the liquid. The relationship between the frequency-dependent impedance $Z_l(\omega)$ and the permittivity ϵ_l of the solution can be expressed as [19, 27]

$$Z_l(\omega) = \frac{K}{j\omega\epsilon_0\epsilon_l(\omega)}, \tag{3}$$

where ϵ_0 is the permittivity of free space, and K is the cell constant. As a result, the permittivity corresponding to different concentration levels can be inferred by measuring the impedance of the solution.

3 PRELIMINARY STUDY OF BASIC METASURFACE UNIT

To fully leverage the impedance variations induced by solute concentration differences, we design a basic metasurface unit that serves as the initial sensing interface. This metasurface functions as a resonant structure that amplifies and captures subtle permittivity variations, effectively converting minute permittivity changes into detectable spectral signatures. Compared to conventional RF reflection-based sensing, where weak variations are often obscured by signal attenuation, this approach significantly improves the sensing signal-to-noise ratio.

The basic unit structure is presented in Fig. 3(a), which consists of a three-layer configuration: a metallic resonant surface, a dielectric substrate, and a copper ground plane. To analyze the interaction between the metasurface and the liquid medium, we employ the equivalent circuit model as shown in Fig. 3(b). In this model, the surface geometry is characterized by an equivalent capacitance C_1 and inductance L_1, while Z_s represents the

substrate impedance. Following the analytical formulations in [4, 33], C_1 and L_1 are determined by:

$$C_1 = \frac{\epsilon_0 \epsilon_r (r_1 - r_0) h}{d}, \quad L_1 = \frac{\mu_0 \pi r_0^2}{h}, \tag{4}$$

where ϵ_0 and μ_0 are the permittivity and permeability of free space, respectively. ϵ_r denotes the relative permittivity of the substrate. The geometric parameters r_0 and r_1 denote the inner and outer radii, while h and d correspond to the substrate thickness and gap width, respectively.

Directly measuring liquid impedance is impractical outside laboratory settings as it requires specialized equipment and is prone to measurement errors. Specifically, electrode–liquid interface polarization and contact instability often introduce measurement drift and poor repeatability, hindering accurate characterization of the liquid's dielectric properties. To overcome these limitations, we model the liquid as an equivalent load Z_l that is electromagnetically coupled to the metasurface, enabling wireless sensing via RF signals. As shown in Fig. 3(b), Z_l represents the equivalent load impedance introduced by the liquid in direct contact with the metasurface. Since the liquid's permittivity primarily affects the capacitive response, its impact on the inductance is negligible in this model, yielding $L_{total} \approx L_1$ [7, 12, 23]. Consequently, the liquid loading can be modeled as a capacitor $C_l = \epsilon_l C_0$, where C_0 is the geometric capacitance determined by the electrode geometry in free space [15]. Under fixed geometry, C_0 is treated as a constant parameter. Under these conditions, variations in the liquid permittivity ϵ_l modify the total equivalent capacitance, thereby shifting the metasurface resonance frequency f_r [23, 24, 51]:

$$f_r = \frac{1}{2\pi\sqrt{L_1(C_1 + C_s + C_l)}} = \frac{1}{2\pi\sqrt{L_1(C_1 + C_s + \epsilon_l C_0)}}, \tag{5}$$

where C_s denotes the equivalent capacitance of the substrate. Hence, by tracking the resonance frequency shift in the reflected signal, the metasurface enables estimation of contaminant concentration levels in liquid samples.

4 PASSIVE METASURFACE DESIGN

This section presents our metasurface design, which focuses on three key aspects: (i) addressing the sensitivity limitations of conventional frequency-shift-based methods, (ii) enhancing sensing sensitivity, and (iii) enabling multi-dip information encoding through the resonance splitting effect.

4.1 Addressing Sensitivity Limitations in Frequency-Shift-based Method

While conventional frequency-shift–based approaches leverage resonance frequency shifts to detect permittivity changes, the resulting frequency shift is insufficient to resolve ultra-low concentration variations. Specifically, subtle changes in liquid concentration do not induce a discernible shift in the frequency spectrum. As shown by the simulation in Fig. 4, we analyze the reflection coefficient of a basic split-ring metasurface operating at 7.4 GHz with pure water. After introducing 5 ppm lead ions (Pb^{2+}), the resonance frequency (i.e., reflection dip) remains unchanged, indicating limited sensitivity to low-concentration contaminants.

Furthermore, the frequency resolution of commercial UWB radar is limited to 15.2 MHz [34]. As a result, concentration changes can only be detected when the induced resonance shift exceeds this threshold. In practice, ppb-level concentrations typically produce shifts far smaller than this 15.2 MHz bin, making them undetectable. Consequently, conventional frequency-shift–based approaches lack the resolution needed to capture fine-grained concentration variations.

Improving sensitivity through amplitude and phase. To address the limited sensitivity of frequency-shift-based methods, we move beyond tracking a single resonance frequency shift. Instead, we exploit both the

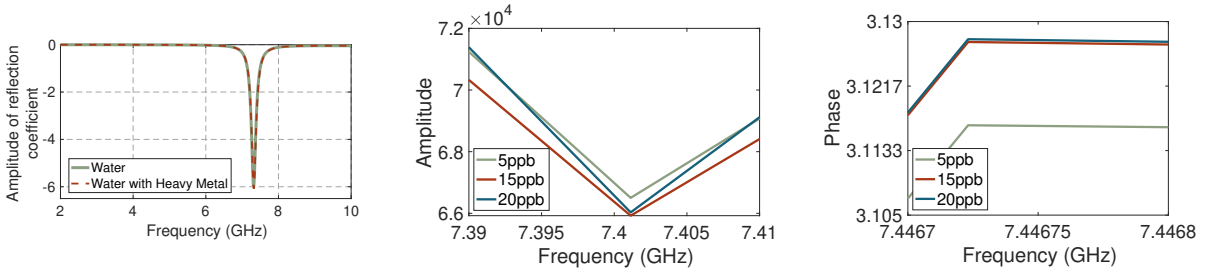

Fig. 4. Simulation-based comparison between pure water and aqueous solutions with 5 ppm heavy metal contamination, followed by real-measurement amplitude and phase variations at the ppb level under different Pb concentrations.

amplitude and phase characteristics of the reflected signal, which are highly sensitive to subtle variations in contaminant concentration.

To extract these multidimensional features using UWB radar, we transform the received channel impulse response (CIR) signal into the frequency domain to obtain the frequency response $H(f)$, which can be expressed as [11]:

$$H(f) = \int_{-\infty}^{\infty} h(t)e^{-j2\pi ft}dt = |H(f)|e^{j\phi(f)}, \tag{6}$$

where $|H(f)|$ denotes the magnitude and $\phi(f)$ represents the phase of frequency response.

To evaluate the sensitivity of these frequency-domain characteristics, we analyze the amplitude and phase responses of the signals reflected from a basic split-ring metasurface. This analysis is conducted with the metasurface in direct contact with lead (Pb^{2+}) solutions at concentration levels of 5, 15, and 20 ppb. As shown in Fig. 4, the spectral region around the designed resonance dip exhibits clear distinctions between 5 ppb and 20 ppb concentrations in both amplitude and phase domains, even though the resonance frequency shifts are indistinguishable. Specifically, the amplitude response varies with concentration, and the phase value exhibits a subtle shift in the phase transition point. This transition point corresponds to the frequency region where the resonance-induced phase rapidly changes by approximately π. These variations arise from concentration-induced changes in the liquid's permittivity, which modify the local electromagnetic field and shift the resonance condition. Notably, the amplitude minimum and the phase transition point do not occur at exactly the same frequency, reflecting different sensitivities of amplitude and phase responses to permittivity variations. This provides complementary spectral information that enhances both robustness and sensing resolution. These observations highlight the importance of jointly analyzing amplitude and phase features, which renders the discrimination of ppb-level concentration variations feasible despite limited frequency resolution.

Overall, these results demonstrate the potential of leveraging amplitude–phase features to replace the frequency-shift-based method for ppb-level water contaminant detection. However, the basic split-ring structure remains insufficient to reliably distinguish closely spaced concentration levels at the ppb scale. As shown in Fig. 4, the spectral responses for 15 ppb and 20 ppb lead concentrations exhibit substantial overlap in both amplitude and phase domains. This high degree of spectral similarity makes these levels prone to mutual interference, thereby blurring the detection boundary and limiting the overall sensing resolution.

These limitations motivate us to evolve the metasurface design to enhance discrimination capability through two complementary strategies: (i) maximizing amplitude-phase sensitivity within a single resonance dip to resolve fine-grained concentration variations, and (ii) leveraging multiple resonance dips to encode additional discriminative features within the limited bandwidth of commercial UWB devices, thereby improving robustness under complex real-world environments.

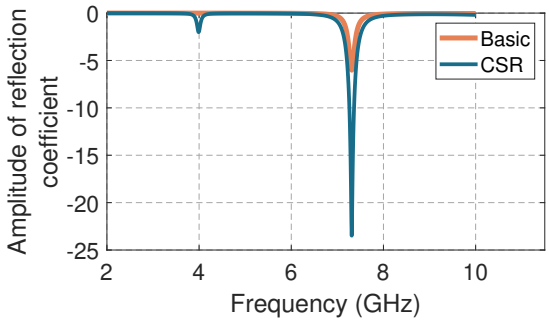

Fig. 5. Amplitude of reflection coefficient for basic and CSR structure.

4.2 Amplifying Sensitivity within a Single Resonance Dip

In this section, we enhance sensitivity within a single resonance dip by designing a Complementary Split-Ring (CSR) structure.

Our basic idea is to improve the depth and sharpness of the resonance dip to maximize the contrast induced by subtle permittivity variations in the spectrum, thereby encoding more contaminant-specific information into the reflected signal. As shown in Fig. 5, these resonance characteristics are reflected in the reflection coefficient S_{11}, where depth denotes the magnitude of peak attenuation and sharpness represents the steepness of the spectral variation. A sharper and deeper resonance increases spectral contrast, specifically the magnitude and phase differentiation between different concentration levels, thereby enhancing the system sensitivity to subtle changes in the liquid's composition.

To improve sensitivity and enrich the encoded information in the resonance dip, we implement a CSR structure [33], as shown in Fig. 6(a). While CSR configurations are well-established in metamaterial and antenna design, to the best of our knowledge, this is the first work to leverage such a structure for fine-grained liquid sensing. The CSR design leverages a dual-ring configuration to deepen the resonance dip through mutual coupling between the inner and outer rings [4]. This transition from a single split-ring to a CSR structure is designed to significantly sharpen the resonance while maintaining the target operating frequency band. The electromagnetic interaction between the rings can be quantified by a mutual coupling coefficient $m \approx (f_2^2 - f_1^2)/(f_2^2 + f_1^2)$, where f_1 and f_2 denote the intrinsic resonance frequencies of the individual rings. This coupling effect determines the separation and depth of the resulting resonant dips.

To quantitatively characterize the sharpness of resonance, we adopt the dimensionless quality factor, $Q = f_r/\Delta f$, where Δf represents the full width at half maximum (FWHM). A higher Q factor corresponds to a sharper resonance. As shown in Fig. 5, the basic single-ring design exhibits a 6 dB resonance dip with a Q factor of 45.7. In contrast, the CSR-enhanced structure achieves a significantly deeper resonance dip (14 dB) along with a much higher Q factor of 253, leading to improved spectral contrast for resolving ppb-level concentration variations.

The increased Q factor amplifies the sensitivity of both amplitude and phase responses to permittivity variations, thereby enlarging the separation between concentration-dependent signals. While high-Q structures are typically more susceptible to environmental noise, the CSR design mitigates this issue through strong electromagnetic field confinement. By confining electromagnetic energy within the substrate-metal interface, the structure reduces the influence of ambient disturbances, such as small temperature drift and nearby movements. As a result, the CSR-enhanced design improves the spectral resolution of the frequency response $H(f)$ while maintaining robustness in practical deployment scenarios.

Building upon the enhanced resonance characteristics, we define each resonance dip as an *information-rich dip*, as it exhibits improved sensitivity to concentration-induced perturbations. To quantify this sensitivity, we adopt

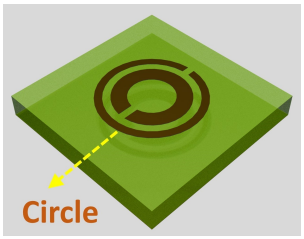

(a) Complementary Split-Ring (CSR)

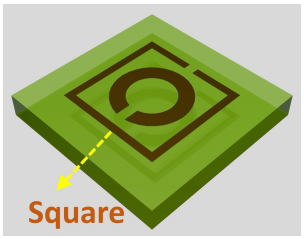

(b) Partial Symmetry Square

(c) Complementary Asymmetric Split Square (CASS)

Fig. 6. Design evolution of metasurface unit cell.

a multivariate discriminant metric based on Hotelling's T^2 criterion [21, 30], which jointly captures amplitude and phase variations:

$$S_T(f_i) = (\boldsymbol{\mu}_{\text{high}} - \boldsymbol{\mu}_{\text{low}})^\top \Sigma^{-1}(f_i)(\boldsymbol{\mu}_{\text{high}} - \boldsymbol{\mu}_{\text{low}}), \tag{7}$$

where $\boldsymbol{\mu}_{\text{high}} = [\,\overline{A}_{\text{high}}(f_i), \overline{\Phi}_{\text{high}}(f_i)\,]^\top$ and $\boldsymbol{\mu}_{\text{low}} = [\,\overline{A}_{\text{low}}(f_i), \overline{\Phi}_{\text{low}}(f_i)\,]^\top$ denote the mean amplitude-phase vectors of the high- and low-concentration samples, respectively. $\Sigma(f_i)$ represents their joint covariance matrix, which captures both the noise level and the correlation between amplitude and phase. This metric effectively measures the Mahalanobis distance [16] between concentration-induced responses, highlighting frequencies where amplitude and phase variations are both strong and consistent across samples. Therefore, it provides a principled way to identify spectral regions that carry the most discriminative information.

Based on the equation, we identify an *information-rich band*, i.e., a frequency region where $S_T(f)$ is maximized and the reflected signal exhibits high information density. Within the *information-rich band*, both amplitude and phase responses are highly sensitive to variations in liquid composition. However, relying solely on an extremely high Q factor at a single resonance dip offers marginal improvement, as excessive sharpening reduces robustness to environmental noise and system variations. This limitation motivates a shift in design strategy: instead of further sharpening a single dip, we enhance the overall system sensitivity by introducing multiple information-rich dips.

4.3 Resonance Splitting-enabled Multi-dip Spectral Encoding

To overcome the limitations of single-dip sensing, we introduce a resonance splitting-enabled multi-dip spectral encoding scheme to increase the effective information capacity within a fixed bandwidth. Drawing inspiration from Shannon's capacity theorem [31, 39], the extractable sensing information is governed by the usable spectral bandwidth and signal quality. While our previous analysis established a link between permittivity variations and amplitude–phase responses, a single resonance dip provides limited capacity for ppb-level discrimination. Given that the bandwidth of commercial UWB radar is fixed, further improvements in sensing resolution must rely on increasing the effective information density rather than expanding the bandwidth. To this end, we introduce multiple *information-rich dips* within the available frequency band, where each dip acts as an independent spectral carrier encoding target-specific permittivity variations.

To realize this multi-dip encoding scheme within a constrained bandwidth, we propose a metasurface design based on *resonance splitting*, where a single resonance dip divides into two or more distinct dips due to mutual mode coupling or structural asymmetry [13, 47, 54]. This approach creates two information-rich dips within the existing UWB band, effectively increasing information encoding capacity without introducing additional spectral

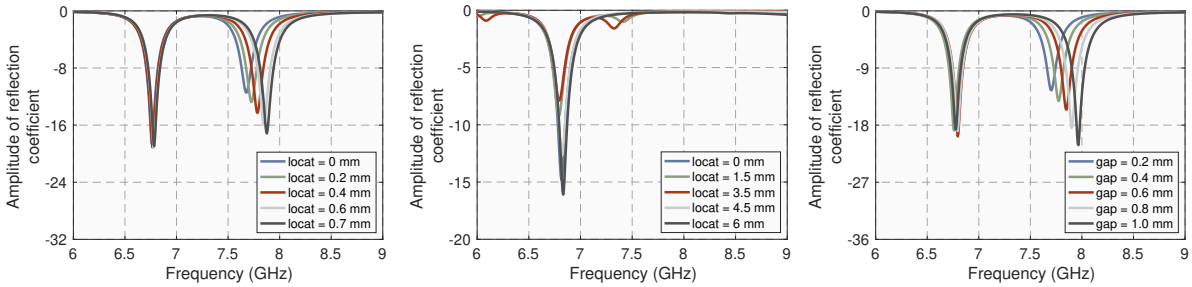

(a) Gap Located on the Side Edge (b) Gap Located on the Opposite Edge (c) Gap Size Variation

Fig. 7. Simulation-based parameter sweep illustrating the design exploration of the CASS structure.

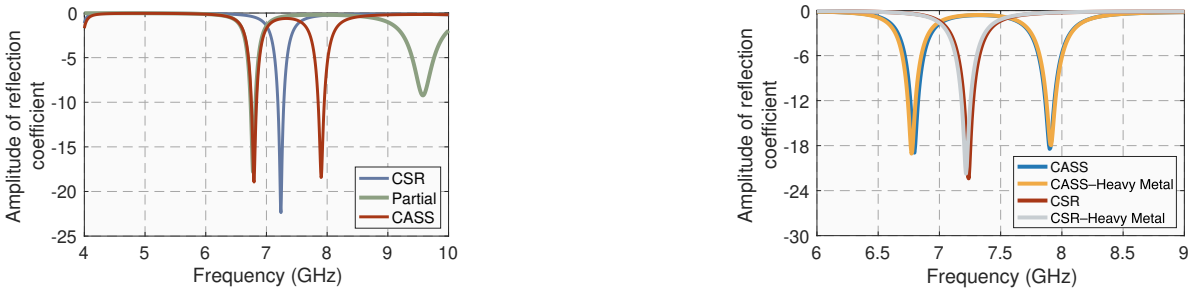

(a) Comparison of Different Surface-Layer Structures

(b) Comparison Between CSR and CASS Under Heavy-Metal Loading

Fig. 8. Simulation results for different metasurface design options.

overhead. Although resonance splitting sometimes can lead to unpredictable shifts or Q-factor reduction, these effects can be mitigated with properly configured designs, rendering the technique highly advantageous [13, 54].

Building upon the resonance splitting mechanism, we next identify three structural factors regulating resonance splitting: (i) resonator coupling strength, (ii) geometric asymmetry of the surface layer, and (iii) spatial discreteness induced by gap placement. Fig. 6 shows the evolution from a standard CSR to our final configuration. To investigate the effect of geometric asymmetry while largely preserving coupling strength, we replace the outer circular resonator with a square frame of comparable perimeter, as shown in Fig. 6(b). This modification introduces controlled geometric asymmetry without substantially altering the average coupling distance. However, the resulting nonuniform spacing between the square and the inner ring leads to spatially varying mutual coupling. This perturbation modifies the effective coupling matrix $\mathbf{M}'$, causing a shift in the original resonance dip $S_{11}(f_1)$ and the emergence of a secondary dip $S_{11}(f_2)$, as indicated by the green curve in Fig. 8(a).

However, although geometric asymmetry can induce resonance splitting, the resulting resonance dip remains weak and often falls outside the effective operating band of the UWB radar, leading to limited attenuation and reduced spectral sensitivity $S(f)$. This indicates that asymmetry alone is insufficient to achieve strong field confinement and deep resonance necessary for robust sensing. To address this, we introduce spatial discreteness by incorporating a narrow gap into the outer square resonator, transforming the partially asymmetric design into a fully asymmetric configuration, termed the Complementary Asymmetric Split Square (CASS) structure, as shown in Fig. 6(c). This gap acts as a capacitive discontinuity, introducing an additional reactive element that enables the formation of a well-defined secondary resonance. By combining geometric asymmetry with gap-induced spatial

discreteness, the CASS structure achieves stable resonance splitting with sufficient attenuation at both resonance dips, as shown in Fig. 8(a). This design fully exploits the available UWB spectrum by activating previously underutilized frequency regions as an additional information-rich dip.

To systematically control the resonance splitting behavior introduced by the CASS structure, we formulate an optimization objective to balance the attenuation depth and spectral symmetry of the two split resonance dips. Guided by these design requirements, we jointly optimize the gap width and its spatial location to achieve stable and well-balanced dual-dip responses:

$$\begin{aligned}(d^*, x^*, y^*) = \underset{d,x,y}{\text{argmax}} \, [&\min\left(S_{11}(f_1), S_{11}(f_2)\right) \\ &- \lambda |S_{11}(f_1) - S_{11}(f_2)|],\end{aligned} \tag{8}$$

where $S_{11}(f)$ denotes the reflection coefficient at frequency f, d represents the gap width, and (x, y) defines the starting location of the gap within the surface-layer coordinate system. The parameter λ controls the tradeoff between maximizing resonance depth and maintaining spectral symmetry. In this optimization, the inner resonator radius and outer square dimensions are fixed to stabilize the operating frequency, while the gap width d and its location (x, y) serve as the primary design variables regulating the resonance splitting behavior.

For the physical implementation of the CASS design, the unit cell is constructed with a compact footprint of 12 mm $\times$ 12 mm. The circular resonator features an outer radius of 2.6 mm and an inner radius of 1.6 mm, while the outer square frame has an edge length of 7.5 mm. These geometric parameters are selected to place the primary resonance within the UWB operating band around 7.3 GHz. Although the overall structure is geometrically scalable to different UWB frequency ranges, precise re-tuning is required due to the non-linear dependence of the effective permittivity on substrate, ground plane, and liquid loading effects. Importantly, such fine-tuning is confined to a small local parameter space, allowing the proposed optimization to converge rapidly. As a result, the proposed CASS design can be adapted to different UWB platforms with only minor parameter adjustments, without requiring structural redesign.

To identify the optimal design parameters, we systematically explore the impact of gap placement on resonance splitting behavior and sensing performance. As shown in Fig. 7(a), placing the gap on the left edge with an offset of 0.7 mm produces the most favorable configuration, in which the secondary resonance dip is shifted toward the upper boundary of the UWB band, aligning well with the operating range of commercial UWB radar. This configuration also achieves the strongest overall attenuation across both resonance dips and is therefore adopted in subsequent experiments. In contrast, placing the gap on the opposite edge, as shown in Fig. 7(b), disrupts the original resonance mode and leads to the formation of a weak secondary dip with significantly reduced attenuation, resulting in degraded sensing performance. Finally, we perform a systematic gap-width sweep as guided by Eq. 8, as shown in Fig. 7(c). The results indicate that $d = 0.8$ mm yields two resonance dips with well-balanced attenuation depths, enabling balanced information contribution from both channels and maximizing effective information density. Considering fabrication constraints with a 0.1 mm resolution, we adopt $d = 0.8$ mm as the final design choice, balancing spectral performance and manufacturability.

The final simulation results presented in Fig. 8(a) confirm the effectiveness of the optimized CASS design. These results clearly illustrate that the original resonance dip is successfully split into two distinct and well-confined resonances within the UWB band. This outcome demonstrates that the CASS structure effectively redistributes spectral resources, enabling the encoding of previously underutilized frequency regions while maintaining strong resonance sharpness and attenuation. Fig. 8(b) further evaluates the CASS and CSR responses under heavy-metal contamination, consistent with the simulation settings in Fig. 4. While both designs significantly outperform the basic split-ring structure, the CASS structure achieves superior information density; its dual-dip profile effectively captures multi-dimensional spectral variations, providing complementary rather than redundant spectral features.

These results confirm that multi-dip encoding provides richer and more discriminative spectral representations of contaminant variations.

In conclusion, the CASS structure shifts the design focus from overly sharpening a single resonance to expanding the effective spectral feature space. Each split resonance serves as an independent channel, encoding liquid-induced perturbations with distinct sensitivities. This multi-dip strategy enhances the overall system distinguishability without relying on excessively high Q factors that might compromise environmental robustness. As a result, it establishes a more expressive and robust sensing framework for reliable water contamination detection in complex real-world environments.

5 WATER CONTAMINANT PREDICTION

This section details our signal processing and inference framework for ppb-level water contaminant prediction. We first extract amplitude and phase features from the reflected UWB signals, and then leverage their first-order derivatives to mitigate multipath effects and align the resulting spectral profiles. Based on these processed features, we develop an interpretable regression model for contaminant quantification, with model parameters visualized for representative heavy-metal contaminants, including copper (Cu) and lead (Pb).

5.1 Amplitude and Phase of Reflection Coefficient Extraction

As indicated in Sec. 4.1, the amplitude and phase of the complex reflection coefficient are key indicators of the interaction between the metasurface and the aqueous solution. To extract these characteristics, we analyze the received UWB signals in the frequency domain to recover these characteristics over the target spectrum. The measured amplitude $|H(f)|$ and phase $\phi(f)$ can be modeled by Eq. 9 [48, 53]:

$$\begin{cases} |H(f)| \propto |H_{trans}(f)| \cdot |H_{prop}(f)| \cdot |S_{11}(f)|, \\ \phi(f) = \phi_{trans}(f) + \phi_{prop}(f) + \phi_{meta}(f), \end{cases} \tag{9}$$

where $H_{trans}(f)$ and $\phi_{trans}(f)$ represent the initial amplitude and phase of the transmitted signal, $|S_{11}(f)|$ and $\phi_{meta}(f)$ capture the effect of the metasurface on signal propagation, $|H_{prop}(f)|$ and $\phi_{prop}(f)$ denote the propagation effects. Among these factors, multipath propagation contributes most significantly to environmental distortion in practical scenarios.

5.2 Recognition Pattern Selection

In this section, to improve the concentration resolution and maximize the bandwidth utilization efficiency, we select informative regions from both the amplitude and phase components of the frequency spectrum $H(f)$. We focus on informative spectral regions while suppressing noisy and redundant frequency components, thereby reducing computational overhead and improving robustness for contaminant discrimination.

The selection process naturally begins with a focus on the most prominent features, typically by treating the entire resonance dip as the primary sensing pattern. However, two major challenges remain. First, to ensure system stability and prevent false detections, the selected spectral regions must exhibit sufficient robustness under diverse real-world conditions. Both the amplitude and phase components of $H(f)$ are highly sensitive to environmental interference. In particular, complex multipath effects can distort the propagation channel response $H_{\text{prop}}(f)$, thereby altering the observed frequency spectrum $H(f)$ at the receiver. Second, there exists an inherent frequency misalignment between amplitude and phase features, which we will address after mitigating multipath-induced distortions.

To evaluate the impact of multipath interference, we conduct a controlled experiment, as shown in Fig. 9(a). In this setup, a UWB radar module transmits and receives signals directed toward a metasurface-embedded cup placed within its line-of-sight (LoS). The metasurface is embedded on the outer surface of a white container

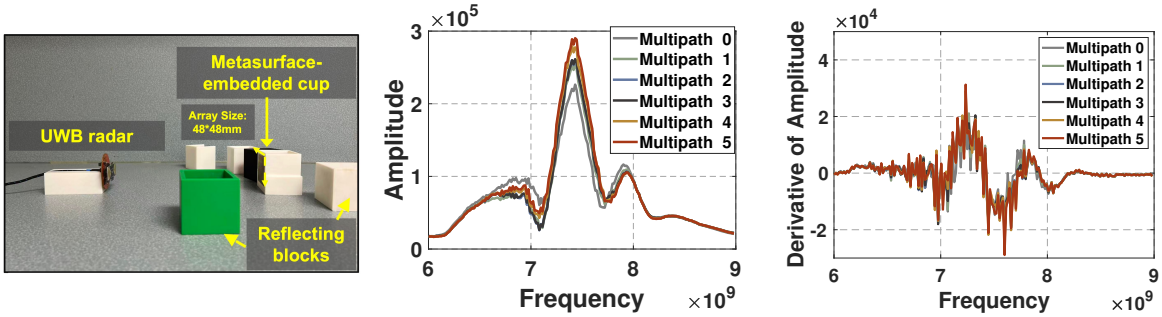

(a) Controlled experiment setup to analyze the impact of multipath interference

(b) Amplitude Variation

(c) Derivative of Amplitude

Fig. 9. Multipath effects and mitigation method.

filled with the test liquid, while several surrounding blocks, made of the same material but in different sizes, are arranged to emulate reflections from nearby objects. Additionally, the desk surface introduces a consistent reflection across all test conditions, serving as a baseline multipath component. We define a baseline configuration, *Multipath 0*, where only the target cup is present along the LoS. As the number of surrounding reflective blocks increases from one (*Multipath 1*) to five (*Multipath 5*), multiple reflection paths emerge, leading to noticeable fluctuations in the amplitude response $A(f)$, as shown in Fig. 9(b). These multipath-induced variations distort spectral consistency and compromise signal reliability, thereby degrading the stability and distinctiveness of the identified information-rich dips.

Beyond environmental robustness, the inherent frequency misalignment between amplitude and phase presents another key challenge. While the amplitude–phase misalignment increases the information richness of the reflected spectrum by providing complementary features, it also complicates the selection of informative regions. As presented in Fig. 10(a), amplitude resonance dips and phase transition points are misaligned. This lack of synchronization makes it challenging to identify and bound the same information-rich regions across different features, particularly when they are jointly leveraged for target detection. Taken together, the dual challenges of multipath-induced instability and cross-feature misalignment necessitate a more robust and unified pattern representation to ensure reliable sensing.

To address these issues, we leverage the spectral derivatives of amplitude and phase, i.e., $\frac{d(A(f))}{df}$ and $\frac{d(\phi(f))}{df}$, as key recognition patterns. These derivatives inherently capture local spectral transitions while mitigating absolute value shifts caused by environmental variations, enabling more stable and discriminative feature extraction across diverse scenarios. As shown in Fig. 9(c), the amplitude derivatives $\frac{d(A(f))}{df}$ across various multipath conditions remain tightly clustered within a narrow frequency range, underscoring the system's robustness to interference caused by surrounding environmental objects. This robustness stems from the inherent characteristics of the passive metasurface, which induces sharp amplitude gradients within the resonance dips, producing pronounced derivative peaks that are clearly distinguishable from background fluctuations. In contrast, multipath effects introduced by nearby objects typically cause gradual or smooth amplitude variations, as shown in Fig. 9(b), which result in near-zero or weakly fluctuating derivatives. This distinction enables the derivative-based representation to reliably suppress multipath-induced distortions while preserving the salient sensing features.

Computing the derivative of both amplitude and phase with respect to frequency provides a more sensitive measure of spectral variation induced by changes in contaminant concentration. While the raw amplitude and phase spectra primarily reflect the overall resonance characteristics, their first-order derivatives highlight the local rate of change in the spectral response. Since concentration-induced dielectric perturbations often cause

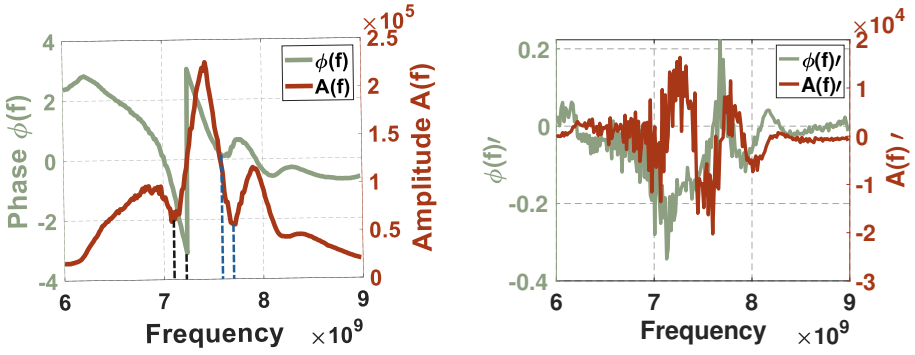

(a) Phase and Amplitude (b) Derivative of Phase and Amplitude

Fig. 10. Feature misalignment and the phase-amplitude alignment process.

subtle frequency shifts or distortions around the resonance dips, these effects manifest more prominently in the derivative domain as sharp peaks or inflection points. Therefore, analyzing $\frac{dA}{df}$ and $\frac{d\phi}{df}$ enhances the contrast between different concentration levels, suppresses low-frequency background variations, and yields a clearer and more robust characterization of concentration-dependent spectral dynamics.

Moreover, as shown in Fig. 10(b), the derivatives of amplitude $\frac{d(A(f))}{df}$ and phase $\frac{d(\phi(f))}{df}$ exhibit substantially improved alignment across the frequency spectrum. Compared to their original forms in Fig. 10(a), where the amplitude dip and phase transition point appear at different frequencies, the derivative curves reveal closely synchronized peaks and transitions. This derivative-based representation also helps eliminate ambiguity caused by gradual or unclear phase transitions in $\phi(f)$. By converting smooth shifts into sharp peaks, $\frac{d(\phi(f))}{df}$ better reflects the underlying spectral variations and aligns more consistently with $\frac{d(A(f))}{df}$. The resulting synchronization enhances feature consistency between amplitude and phase, thereby improving the robustness and precision of resonance-based pattern recognition.

To capture fine-grained spectral variations more effectively, we refine the original function $S_T(f_i)$ by incorporating the first-order derivatives of amplitude and phase. This modification emphasizes the local slope of the spectral response, where concentration-induced perturbations are most pronounced. The refined metric, $S'_T(f_i)$, integrates derivative-based contrasts in both domains:

$$S'_T(f_i) = \alpha \cdot \frac{\left|\Delta\overline{A'}(f_i)\right|}{\sigma_{A'}(f_i)} + \beta \cdot \frac{\left|\Delta\overline{\Phi'}(f_i)\right|}{\sigma_{\Phi'}(f_i)}, \tag{10}$$

where $\Delta\overline{A'}(f_i)$ and $\Delta\overline{\Phi'}(f_i)$ denote the differences between the mean spectral derivatives of amplitude and phase between concentration groups at frequency f_i, respectively, $\sigma_{A'}(f_i)$ and $\sigma_{\Phi'}(f_i)$ represent their corresponding standard deviations across samples. Weighting coefficients α and β balance the contributions of each feature. This derivative-enhanced formulation maintains the statistical rigor of Eq. 7 while highlighting spectral regions that exhibit both high discriminability and steep resonance gradients, providing a more robust indicator of frequency-dependent sensitivity.

Building on this refined metric, we define an information-rich band as a contiguous set of frequency points where the sensitivity $S'_T(f_i)$ exceeds a predefined threshold γ:

$$\text{band}_j = \{\, f_i \mid S'_T(f_i) > \gamma \,\}, \quad j \in \{1, 2\}, \tag{11}$$

where each band_j corresponds to a distinct spectral region containing strong and consistent concentration-dependent responses. In practice, the two prominent resonance dips observed in the reflection spectrum form

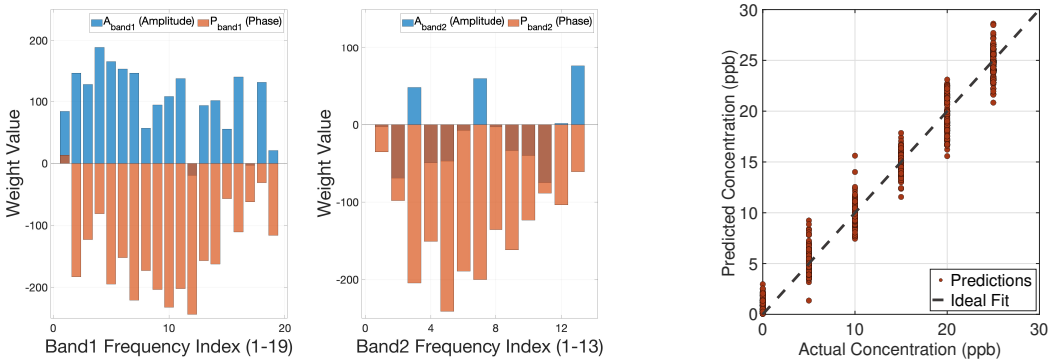

(a) Band1 & 2 Weights for Cu (b) Regression Model - Cu

Fig. 11. Weight parameters and R^2 for Cu.

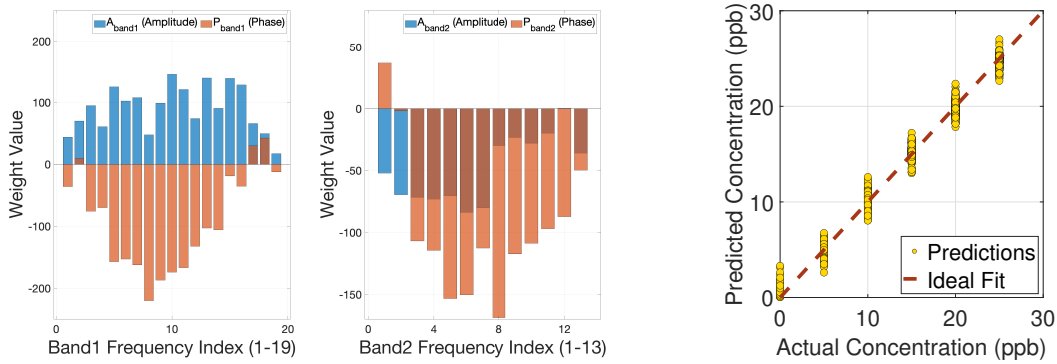

(a) Band1 & 2 Weights - Pb (b) Regression Model - Pb

Fig. 12. Weight parameters and R^2 for Pb.

two separate information-rich bands, denoted as band_1 and band_2. This formulation enables the data-driven extraction of robust and high-resolution sensing features from the most informative spectral segments, which are subsequently fed into the regression model for quantitative water contamination analysis.

5.3 Physically Interpretable Model for Liquid Identification

To further validate the feasibility of our passive metasurface–based contaminant level quantification and explain the underlying sensing mechanism, we model the concentration level $\hat{C}$ of the target element t using a physically interpretable regression framework. This model employs a discretized weighted summation of the spectral derivatives of amplitude and phase, jointly integrating features from the two distinct information-rich bands identified in Sec. 5.2.

$$\begin{aligned}\hat{C}_t = &\sum_{i=1}^{n_1} \left[a_i \cdot A'_{band1}(f_i) + c_i \cdot \Phi'_{band1}(f_i)\right] \\ &+ \sum_{j=1}^{n_2} \left[b_j \cdot A'_{band2}(f_j) + d_j \cdot \Phi'_{band2}(f_j)\right],\end{aligned} \tag{12}$$

where $A'_{band1}(f_i)$ and $\Phi'_{band1}(f_i)$ denote the amplitude and phase derivatives at frequency point f_i within the first information-rich band, and $A'_{band2}(f_j)$ and $\Phi'_{band2}(f_j)$ are defined analogously for the second band. The coefficients a_i, b_j, c_i, and d_j represent the weights associated with each spectral component in predicting $\hat{C}_t$.

Fig. 11(a) and Fig. 12(a) demonstrate the distribution of weighting coefficients assigned to individual frequency points across the two bands for Copper (Cu) and Lead (Pb) concentration prediction. A total of 32 frequency points, including 19 from band_1 and 13 from band_2, are selected from a 500 MHz bandwidth. To ensure a balanced contribution within the regression framework and enable stable optimization, the derivatives of amplitude and phase are normalized to the same scale.

The distinct distribution patterns of selected points in band_1 and band_2 further indicate that these bands provide distinguishable and complementary contributions to the prediction task. This observation highlights the effectiveness of our resonance splitting and multi-dip encoding strategy in capturing non-redundant spectral features that are highly relevant to the target analytes. Regarding amplitude and phase features, their different sensitivities to concentration-induced permittivity variations enable the model to access richer concentration-dependent spectral information. By jointly leveraging derivatives from both features, the system achieves higher robustness and sensing resolution. The prediction results of the linear regression model are presented in Fig. 11(b) and Fig. 12(b), achieving R^2 values of 0.9718 for Copper and 0.9875 for Lead. These high coefficients of determination validate the model's ability to accurately capture ppb-level concentration variations by leveraging phase and amplitude features extracted from the selected information-rich band.

This interpretable regression model provides clear physical insight into the metasurface-based sensing mechanism. While effective for estimating the concentration of a single contaminant, it does not directly generalize to multi-class scenarios involving multiple substances. To address this limitation, we reformulate the regression model into a shallow neural network–based classification framework. This design preserves the physical interpretability of the extracted features while enabling nonlinear mapping for improved multi-class discriminability. Each liquid sample x_n is represented by a 32-dimensional feature vector $\mathbf{x}_n = [A'_{band1}(f_1), \Phi'_{band1}(f_1), \ldots, A'_{band2}(f_{n_2}), \Phi'_{band2}(f_{n_2})]$, constructed from amplitude and phase derivatives at selected information-rich frequency points. The classification network consists of a single hidden layer that introduces nonlinear feature transformation:

$$\mathbf{h}_n = \sigma(\mathbf{W}_1\mathbf{x}_n + \mathbf{b}_1), \quad \hat{y}_n = \underset{k\in\{1,2,\ldots,K\}}{\text{argmax}} \left(\mathbf{w}_{2,k}^{\top}\mathbf{h}_n + b_{2,k}\right), \tag{13}$$

where $\sigma(\cdot)$ denotes the nonlinear activation (*tansig* in our implementation), and $\mathbf{W}_1$, $\mathbf{b}_1$, $\mathbf{w}_{2,k}$, and $b_{2,k}$ are the learnable parameters. The model outputs class probabilities via softmax normalization and is trained using a cross-entropy loss. By leveraging the same interpretable spectral features as the regression model, this network enables simultaneous identification of contaminant types and concentration levels.

6 IMPLEMENTATION

Passive Metasurface. The passive metasurface used in MetaTap is fabricated using a standard double-sided FR-4 PCB through an electroless copper plating process. The FR-4 substrate has a relative permittivity of $\epsilon = 4.3$ and a thickness of 1.6 mm, with 0.034 mm-thick copper layers on both sides. The total manufacturing cost for a single metasurface unit is less than $0.10. Fig. 13 presents the fabricated metasurface. Since the resonance frequency of the Partial Symmetry Square structure, as shown in Fig. 6(b), falls outside the operating bandwidth of the UWB radar, we adopt three representative structures for evaluation: the basic Split Ring (SR), Complementary Split Ring (CSR), and Complementary Asymmetric Split Square (CASS), corresponding to configurations with one, two, and three resonance dips, respectively. Although the CASS design theoretically supports three resonance

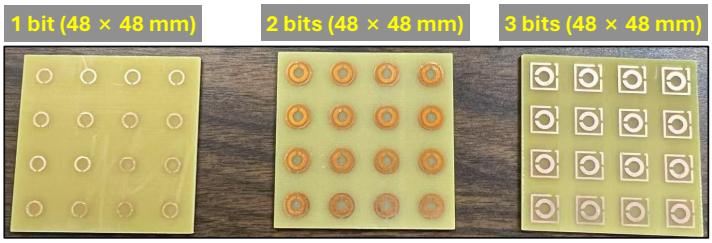

Fig. 13. Surface layer design for passive metasurface.

dips, only the two dominant dips within the effective radar bandwidth are utilized in our experiments to ensure stable and high-SNR spectral responses.

Frontend Hardware. We implement MetaTap using the commercial SLMX4 module [42], which is based on the i.MX RT1060 Crossover MCU with an Arm Cortex-M7 processor from NXP [35] at a price of approximately $150. The module includes 16 MB of flash memory and 8 MB of SDRAM. It is equipped with an elliptical path antenna module (EPAM) that integrates Novelda's X4 UWB impulse radar [34]. The X4 SoC transceiver operates at a central frequency of 7.29 GHz with a bandwidth of 1.4 GHz, and the radar firmware supports a sampling rate of 23.328 GSa/s.

Backend Implementation. We utilize CST Studio Suite [1] for designing, analyzing, and simulating the passive metasurface. We also employ MATLAB and Python for data collection and signal processing. The metasurface geometry is visualized using Blender [6].

7 EVALUATION

Unlike prior wireless liquid sensing studies that primarily evaluate performance under idealized laboratory conditions or coarse classification tasks, our evaluation is explicitly designed around scenarios where existing RF-based approaches are known to degrade or fail. These include fine-grained ppb-level concentration estimation, complex and unknown background compositions, multi-contaminant interference, and variations in container geometry and usage conditions commonly encountered in real-world tap water sensing.

We first establish a controlled reference performance using deionized water, then systematically introduce increasingly challenging conditions, including bandwidth constraints, multipath interference, container variability, unknown concentration levels, contaminant mixtures, and real tap water with unmodeled ionic interference. This evaluation strategy is designed to probe the limits of prior assumptions and to characterize both the robustness envelope and failure modes of MetaTap under realistic in-the-wild deployment scenarios.

7.1 Experiment Settings

To evaluate the versatility of MetaTap across diverse tap water constituents and real-world scenarios, and ensure that its performance reflects generalization rather than chemical-specific overfitting, we selected six target substances and one ubiquitous ionic interferer and categorized them into four categories:

- **Two common daily constituents**: ethyl alcohol and glucose.
- **One non-harmful ionic species**: Strontium ions (Sr^{2+}).
- **Three regulated heavy-metal contaminants**: lead (Pb^{2+}), copper (Cu^{2+}), and nitrate (NO_3^-).
- **One ubiquitous ionic interferer**: sodium chloride (NaCl).

Furthermore, we discretize the concentration range of each substance into six levels (0, 5, 10, 15, 20, and 25 ppb), following a 5 ppb increment commonly used in contamination threshold studies [36]. For better interpretability and practical assessment, these six levels are further grouped into three general safety categories:

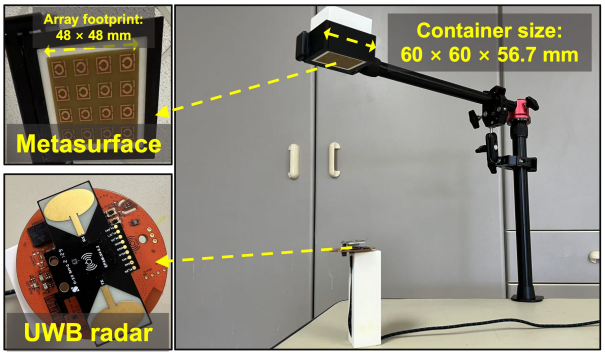

Fig. 14. Experiment setup.

- **Low (Safe)**: ≤ 10 ppb
- **Medium (Warning)**: 10 – 20 ppb
- **High (Dangerous)**: > 20 ppb

All samples are prepared using deionized water, with 0 ppb serving as the baseline reference condition.

Evaluation Model. We evaluate system performance using lightweight neural models that support both classification and regression tasks. Specifically, classification is employed to assess discrete concentration-level identification, while regression evaluates continuous concentration estimation across unknown and intermediate levels. Both models are trained using amplitude–phase derivative features extracted from the dual information-rich resonance bands, which emphasize local spectral variations while suppressing global background drift. This dual evaluation setup goes beyond prior RF-based liquid sensing work that primarily focuses on coarse liquid-type classification, and enables a rigorous assessment of MetaTap in fine-grained ppb-level inference and generalization beyond predefined concentration bins.

Evaluation Metrics. We evaluate system performance using Weighted F1-score and Accuracy. The F1-score is defined as

$$F1 = 2 \times \frac{\text{Precision} \times \text{Recall}}{\text{Precision} + \text{Recall}}, \tag{14}$$

where Precision quantifies the correctness of positive predictions, and Recall measures the ability to identify actual positive instances. The Weighted F1-score is given by

$$\text{Weighted F1} = \frac{1}{\sum_{i=1}^{N} Support_i} \sum_{i=1}^{N} (Support_i \times F1_i) \tag{15}$$

where N denotes the total number of classes, $F1_i$ is the F1-score of class i, and $Support_i$ represents the number of samples belonging to class i. This approach provides a comprehensive evaluation by accounting for the performance of all classes in proportion to their sample sizes. For regression tasks, we evaluate concentration estimation accuracy using the Root Mean Square Error (RMSE).

7.2 Overall Performance

We first evaluate MetaTap under controlled conditions to establish a performance baseline before systematically introducing real-world complexities in subsequent sections. We conduct experiments on six representative substances, i.e., lead (Pb), copper (Cu), strontium (Sr), nitrate, glucose, and ethyl alcohol, across six concentration levels (0 to 25 ppb in 5 ppb increments). The dataset comprises 13,565 samples, partitioned into training and testing

subsets using an 80/20 split. For the structural comparisons among SR, CSR, and CASS designs, the entire pipeline, including data collection, model training, and testing, is conducted independently for each configuration. This design ensures that performance differences reflect intrinsic sensing capability rather than cross-configuration data mixing. Unless otherwise specified, subsequent learning-based evaluations are performed using the optimized CASS configuration.

The setup of MetaTap is shown in Fig. 14. A 4 × 4 CASS metasurface array with a footprint of 48 × 48 mm is integrated at the bottom of a 3D-printed PLA container (60 × 60 × 56.7 mm). The container is positioned approximately 30 cm above the UWB radar module to ensure consistent alignment during measurement. This setup enables stable and repeatable signal acquisition for evaluating both classification and regression performance across different substances and concentration levels.

As depicted in Fig. 15, the unified classification model achieves an overall accuracy of 97.4% across all six substances. Misclassifications are primarily confined to adjacent concentration levels (e.g., 20 ppb vs. 25 ppb for Sr and Pb), indicating that the system maintains high precision even under fine-grained concentration differences. Importantly, no hazardous contaminant is misclassified as a safe constituent, demonstrating strong reliability for safety-critical detection. Furthermore, MetaTap achieves a weighted F1 score of 96.72% and an exceptionally low false positive rate of 0.1%, highlighting its effectiveness in water contamination detection.

	Glucose					Ethyl Alcohol					Sr					Nitrate					Cu					Pb					Water
	5ppb	10ppb	15ppb	20ppb	25ppb	5ppb	10ppb	15ppb	20ppb	25ppb	5ppb	10ppb	15ppb	20ppb	25ppb	5ppb	10ppb	15ppb	20ppb	25ppb	5ppb	10ppb	15ppb	20ppb	25ppb	5ppb	10ppb	15ppb	20ppb	25ppb	0ppb
	1	2	3	4	5	6	7	8	9	10	11	12	13	14	15	16	17	18	19	20	21	22	23	24	25	26	27	28	29	30	31
1	94.1	5.9																													
2		100																													
3		8.3	91.7																												
4			8.3	91.7																											
5				10	90																										
6						100																									
7							93.8	6.2																							
8								100																							
9									100																						
10										100																					
11											100																				
12												100																			
13													100																		
14														92.9	7.1																
15															100																
16																100															
17																	100														
18																		94.1	5.9												
19																			93.8	6.2											
20																				100											
21																					90.5	9.5									
22																						100									
23																							93.3	6.7							
24																								93.3	6.7						
25																									100						
26																										100					
27																										5	95				
28																												100			
29																													100		
30																													4.3	95.7	
31																					1.3					1.3					97.4

Fig. 15. Confusion matrix across all components. The classification follows an order from 5 ppb to 25 ppb for each component: Glucose, Ethyl Alcohol, Sr, Nitrate, Cu, and Pb. The final class, indexed as 31, represents deionized water, corresponding to the 0 ppb concentration level.

7.3 F1-score Comparison Across Different Bandwidth Configurations

To further evaluate the performance of our CASS-based design, we examine the weighted F1-score across various bandwidth configurations. As shown in Fig. 16, the system achieves F1-scores of 95.44% (6 GHz), 94.03% (3 GHz), 95.45% (1.5 GHz), 97.69% (500 MHz), and 88.74% (250 MHz). The best performance at 500 MHz highlights the effectiveness of the CASS design in concentrating highly sensitive features within localized resonance dips. Frequency

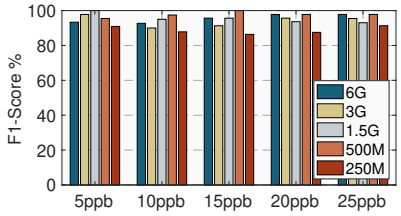

Fig. 16. F1-score across different concentrations and categories.

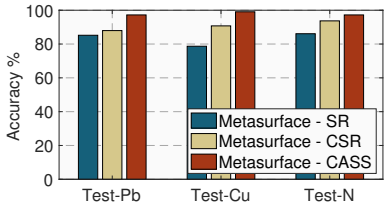

Fig. 17. Impact of different metasurface designs.

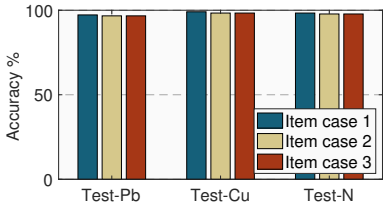

Fig. 18. Impact of multipath.

points within these information-rich regions exhibit pronounced responses to subtle concentration variations, whereas points outside these regions are more susceptible to noise and degrade prediction accuracy. This targeted spectral encoding strategy not only improves detection precision for low-concentration contaminants but also significantly maximizes bandwidth efficiency, demonstrating that high-resolution sensing can be achieved within a compact spectral bandwidth.

7.4 Impact of Metasurface Designs

To demonstrate the performance gains achieved by our metasurface designs, we evaluate three surface-layer configurations in Fig. 13 (from left to right): the basic Split Ring (SR), the Complementary Split Ring (CSR), and the proposed Complementary Asymmetric Split Square (CASS)-based structure.

The experiment results are shown in Fig. 17. We observe that the CSR structure improves average prediction accuracy by 7.47% over the basic SR design, primarily due to its enhanced sensitivity to subtle spectral variations. The CASS design further improves performance by 7.04% by leveraging resonance splitting to introduce an additional information-rich band within the same bandwidth. Overall, the CASS design consistently outperforms the other two configurations, delivering superior discriminative accuracy for Pb, Cu, and nitrate detection in drinking water.

7.5 Impact of Interference from Multipath Effect

To evaluate the robustness of MetaTap against multipath interference, we conduct experiments under three increasingly cluttered scenarios. Case 1 serves as a controlled baseline with a clear line-of-sight and no surrounding objects. In Case 2, one to three reflective objects are placed near the radar at distances comparable to that of the metasurface-embedded container. Case 3 introduces more than three objects randomly placed within the same range to simulate a highly cluttered environment.

Fig. 18 shows that the presence of surrounding reflectors results in negligible performance degradation, with accuracy decreasing by just 0.5%. These results demonstrate that our derivative-based feature extraction effectively filters out the slowly varying environmental reflections, enabling MetaTap to robustly isolate metasurface-specific signatures from complex multipath conditions.

7.6 Impact of Metasurface Array Sizes and Container Shape

In this experiment, we fabricate five prototypes with CASS-based metasurface arrays of varying sizes, ranging from 2×2 to 6×6, to identify the optimal configuration. As shown in Fig. 19, both square and circular container geometries exhibit consistent accuracy trends across these array sizes. Specifically, for square containers, the 4×4 and 5×5 arrays achieve the highest accuracies of 97.22% and 98.61%, respectively. Circular containers show comparable performance with 97.22% for both sizes, indicating minimal sensitivity to container footprint shape. This robustness arises from the fact that MetaTap primarily relies on the effective reflective aperture and full liquid coverage of the metasurface. When the array is fully embedded in a planar base, variations in the container

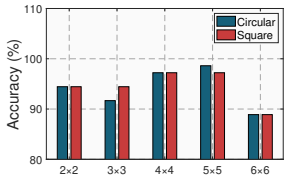

Fig. 19. Impact of array size and container shape.

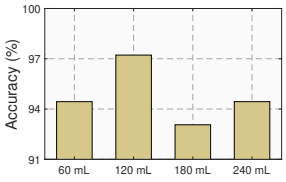

Fig. 20. Impact of liquid volume.

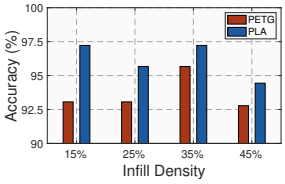

Fig. 21. Impact of material and infill density.

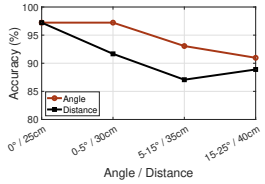

Fig. 22. Impact of different angles and distances.

shape only introduce negligible second-order boundary effects. Furthermore, the resonance-centered features and their local derivatives are inherently resilient to global amplitude scaling and background reflections induced by varying container geometries.

While increasing the array size generally strengthens the reflected signal via constructive combination, the performance is constrained by both internal phase coherence and external geometric matching. Internally, excessively large arrays introduce significant inter-element phase differences, leading to non-coherent superposition or partial destructive interference that degrades signal fidelity. Externally, this degradation is further exacerbated when the array size approaches or exceeds the container base. In such cases, edge truncation and base curvature disrupt the coherent reflection and destabilize resonance responses. Consequently, the primary failure mode of MetaTap arises from phase incoherence and array-to-container geometric mismatch, rather than the container shape itself. To balance sensing precision, robustness, and practical form factors (e.g., standard cup dimensions), we select the 4×4 array as the optimal configuration.

7.7 Practical Considerations

To evaluate the robustness of MetaTap under real-world usage scenarios, we conduct extensive evaluations across three practical dimensions: liquid volume, container material and infill, and sensing geometry (radar-to-target distance and orientation).

Liquid Volume. In practical usage, it is unrealistic to expect users to precisely control liquid volume. To evaluate robustness under volume variation, we conduct experiments with four fill levels: 60 mL (1/4 full), 120 mL (1/2 full), 180 mL (3/4 full), and 240 mL (full). As shown in Fig. 20, MetaTap maintains stable performance across all tested volumes, with classification accuracy consistently above 93.06%. This robustness arises because MetaTap primarily probes the local near-field liquid loading directly above the metasurface. Once the metasurface interface is fully immersed, further increases in volume mainly introduce global amplitude scaling due to changes in path length and attenuation, while the intrinsic resonance modes remain largely unchanged.

Furthermore, the resonance-centered multi-dip features and their frequency-domain derivatives suppress sensitivity to such global shifts while preserving the localized spectral perturbations induced by contaminants. Performance degradation occurs only when the liquid volume is insufficient to fully cover the metasurface, resulting in non-uniform loading and distorted resonance. Within the tested range, the metasurface remains fully immersed, leading to consistently stable performance. These results demonstrate that MetaTap does not require precise volume control from the user, making it well-suited for real-world usage where fill levels naturally vary.

Impact of Container Material and Infill Density. In real-world scenarios, drinking containers are constructed from different materials and structural configurations. Since the metasurface array is embedded in the container base, we evaluate the impact of container material and infill density on system performance. We conduct experiments using two common 3D printing materials, PLA-CF and PETG-CF, across four representative infill densities ranging 15% to 45%.

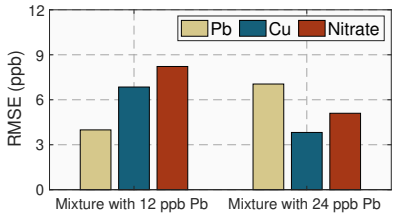

Fig. 23. Concentration estimation performance under contaminant mixture scenarios.

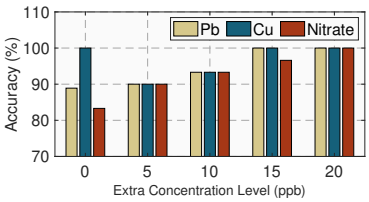

Fig. 24. Interference from tap water

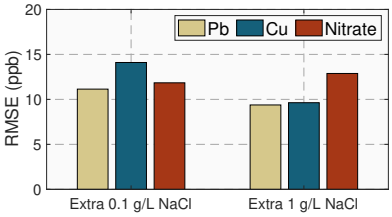

Fig. 25. Interference from tap water and NaCl

Fig. 21 summarizes the sensing accuracy across these configurations. MetaTap maintains consistently high accuracy across both materials and all tested infill densities, with PLA-CF exhibiting slightly higher accuracy than PETG-CF. These material-induced effects primarily manifest as global amplitude and phase baseline shifts, resulting from differences in the effective permittivity and dielectric loss of the container walls. Because these variations introduce background offsets without altering the intrinsic resonance modes, our derivative-based features effectively neutralize such static offsets. This ensures the system to remain sensitive to contaminant-induced perturbations while being robust to variations in container types and fabrication settings.

Angle and Distance. To ensure reliable performance across diverse user habits, we evaluate MetaTap across various distances and angles between the radar and the cup base, as presented in Fig. 22. We observe that as the distance increases and the angle deviates, the sensing performance gradually degrades. In particular, prediction accuracy drops by 10.15% at a distance of 35 cm and by 6.15% when the angle varies from 15° to 25°. Importantly, the system maintains an accuracy above 85% even under these challenging non-ideal conditions. Based on these results, we identify 25 cm and 0° as the optimal operating condition. For practical deployment, we recommend an operational envelope of 25–30 cm with angular variations within ±15° to ensure consistently reliable sensing performance.

7.8 Multi-contaminant Identification and Quantification under Coexisting Interference

To evaluate MetaTap's performance in real-world conditions, we consider mixed contaminants, where multiple substances coexist at unknown, continuous concentrations. We focus on three regulated contaminants: lead (Pb), copper (Cu), and nitrate, which are commonly regulated in drinking water standards. To assess generalization beyond discrete training labels, we evaluate Pb at 12 ppb and 24 ppb, which are excluded from the training set (5, 10, 15, 20, and 25 ppb). For each Pb setting, concentration levels of Cu and nitrate are independently varied over a continuous range from 2.5 ppb to 30 ppb, forming mixed-contaminant samples. During the evaluation, each concentration regression model is trained independently for its target contaminant, without access to other contaminant information. For example, the Pb regression model is trained solely on Pb-labeled data and does not incorporate explicit knowledge of Cu or nitrate concentrations.

Fig. 23 shows the Root Mean Square Error (RMSE) for each contaminant. At 12 ppb of Pb, the RMSEs for Pb, Cu, and nitrate are 3.99 ppb, 6.85 ppb, and 8.22 ppb, respectively. When Pb concentration increases to 24 ppb, the Pb estimation error is 7.05 ppb, while the errors for Cu and nitrate decrease to 3.82 ppb and 5.10 ppb. These results reveal two key observations. First, MetaTap remains capable of jointly estimating multiple contaminants from a single measurement under concurrent interference. Second, lower Pb concentrations reduce the spectral separation among overlapping resonance dips, which increases the susceptibility to cross-interference for Cu and nitrate. This highlights that high sensing resolution is critical for multi-contaminant discrimination, where subtle spectral shifts of individual analytes would otherwise be masked by dominant coexisting signatures. Such

behavior underscores the importance of our multi-dip spectral encoding, which increases information density and enables fine-grained disentanglement of mixed chemical signatures.

Overall, this experiment demonstrates that the improved sensing resolution of MetaTap supports continuous, multi-contaminant concentration inference beyond single-species classification, directly addressing real-world scenarios where contaminant mixtures and unknown concentrations are the norm.

7.9 Interference from Real Tap Water and Complex, Unknown Constituents

This section targets scenarios where prior RF-based liquid sensing systems typically fail, such as unknown background constituents, bulk dielectric drift, and strong ionic interference. Unlike controlled laboratory conditions using pure solvents, real-world tap water is a complex medium containing minerals, residual treatment agents, and dissolved salts. These unknown constituents introduce additional variability into the dielectric environment and pose challenges for accurate contaminant quantification.

To better reflect such in-the-wild conditions, we design two stress-test experiments. First, we manually vary the concentrations of Cu, Pb, and nitrate directly in real tap water, preserving its intrinsic complexity while evaluating system robustness under multi-element interference and sudden contamination changes. Second, we introduce sodium chloride (NaCl) as a ubiquitous yet unobserved interferer during training, serving as a strong out-of-distribution perturbation. NaCl is evaluated at two concentration levels (0.1 g/L and 1 g/L), which substantially exceed typical municipal tap water ionic levels, providing a conservative upper bound on robustness. We intentionally evaluate NaCl concentrations beyond realistic levels to expose failure-adjacent regimes rather than average operating conditions. All regression models are trained without access to tap water or NaCl labels, ensuring a deliberately constrained and realistic evaluation setting.

Interference from Tap Water. As shown in Fig. 24, MetaTap maintains consistent performance under the complex background of real tap water, with an average accuracy of 94.6%. While a modest reduction in accuracy occurs in the low-concentration regime (0–10 ppb), where background interference from tap water constituents has a more pronounced impact on spectral separability, the system still maintains accuracy above 81.9% in these challenging cases. Performance rapidly recovers as contaminant concentrations increase. These results demonstrate that MetaTap remains robust under realistic tap water conditions with complex and unknown background constituents.

Interference from Tap Water and NaCl. Fig. 25 further evaluates the robustness of MetaTap under combined interference from real tap water and a strong out-of-distribution constituent (NaCl). Compared to the case of tap water alone, the introduction of NaCl introduces a strong bulk dielectric perturbation that significantly alters the background electromagnetic environment. Despite this additional interference, MetaTap maintains stable estimation performance for Pb, with RMSE remaining around 9–10 ppb across both NaCl concentration levels. In contrast, Cu exhibits increased sensitivity under higher NaCl concentration, with RMSE rising to 14.10 ppb, indicating stronger feature entanglement under elevated ionic interference. Interestingly, the estimation error for nitrate does not monotonically increase with NaCl concentration, suggesting that its spectral features respond differently to resonance-induced perturbations.

Overall, these results show that while strong and unobserved ionic interference can differentially affect individual contaminants, MetaTap remains robust under severe and unmodeled perturbations. The system preserves stable resonance patterns even under large bulk dielectric and ionic shifts. This indicates that our metasurface encoding is capable of disentangling specific chemical signatures from complex backgrounds, rather than being dominated by global changes in ionic strength or effective permittivity. Notably, the NaCl concentrations evaluated in this study (up to 1 g/L, i.e., ~1000 ppm) substantially exceed typical municipal tap water ionic levels, establishing a conservative upper bound on robustness. Together, these findings highlight

Table 1. Related work in wireless liquid sensing systems.

Work	Radio	Bandwidth	Recognition Pattern	Resolution of Concentration Levels	Applications
TagScan[52]	RFID	4 MHz	Phase & RSS	4-5%	8 Types of Liquids
LiquID[17]	UWB	1 GHz	CIR	5%	33 Types of Liquids
Tagtag[53]	RFID	24.5 MHz	Phase	1% (salt/water)	Liquid and Solid Materials
RF-EATS[20]	RFID	500 MHz	Amplitude & Phase	10%	7 Types of Liquids
FG-LiquID[29]	mmWave	7 GHz	RSS	1% alcohol by volume (ABV)	30 Types of Liquids
Vi-Liquid[22]	Vibration	1.6 kHz	Amplitude	5%	30 Types of Liquids
LiqRay[44]	RF	3.3 GHz	Relative Frequency Response	1%	Alcohol solutions
PackquID[45]	RF	0.9 GHz	Relative Frequency Response	2%	9 Types of Liquids and 4 Types of Packets
LiquImager[43]	RF	5.12 GHz	CSI	1%	8 Types of Liquids and 4 Types of Containers
MetaBioLiq[10]	mmWave	5.5 GHz	Amplitude & Phase	11 ppm (mg/L)	Biofluid

MetaTap's ability to isolate and identify target contaminants under unmodeled background variations, which is critical for practical in-the-wild deployment.

8 DISCUSSION

Impact of Temperature and Ambient Humidity. Temperature plays a critical role in liquid identification, as it directly influences the permittivity of the liquid [9, 26]. Any permittivity-based sensing method, including RF-direct, tag-based, or metasurface-based, is inherently susceptible to temperature-induced permittivity shifts. Similarly, ambient humidity can introduce variability in measurements [49], particularly in sensing configurations where the sample is partially exposed. Fortunately, under typical indoor conditions, the temperature of most drinking water samples remains relatively stable, and humidity fluctuations are minimal. To ensure experimental consistency and minimize environmental variability, all measurements in this study are conducted at a controlled temperature of 25°C under stable ambient humidity conditions.

Smartphone UWB Component. Modern smartphones, such as the iPhone [3], Samsung Galaxy [40], and Google Pixel [37], are equipped with UWB chips operating in the 6–8 GHz range. These components currently support short-range communication and applications such as precision finding and AR-based guidance. However, limited access to raw UWB data and signal attenuation from protective enclosures (e.g., plastic) may constrain certain wireless sensing applications in everyday scenarios. With further development, smartphone-integrated UWB components offer strong potential for practical wireless sensing in daily use.

Impact of Movement in the Sensing Process. Movement of either the radar or the liquid container can affect system performance, as such motions introduce time-varying path distortions and phase inconsistencies that hinder stable frequency-domain feature extraction. For the daily scenario, users are therefore encouraged to keep the container stationary during the sensing period to ensure signal consistency within a one-second acquisition window. In contrast, radar movement offers potential opportunities rather than solely posing challenges. Controlled movement can introduce spatial diversity and enable higher-resolution sensing through synthetic aperture or multi-angle measurements. We leave the exploration of motion-assisted sensing as future work to further enhance the robustness and spatial granularity of the proposed system.

9 RELATED WORK

Wireless Liquid Identification Systems. Wireless liquid sensing offers a non-invasive, portable alternative to liquid identification. As summarized in Table 1, prior RF [17, 22, 29, 43–45], tag-based [20, 52, 53] approaches primarily focus on coarse-grained classification (e.g., 8–33 liquid types) with classification granularity typically limited to 1%. While the state-of-the-art metasurface system [10] achieves ppm-level sensitivity for biofluid using

wideband FMCW radar, it requires significantly higher spectral bandwidth than our approach. In contrast, MetaTap maximizes the constrained bandwidth of commercial UWB transceivers by inducing dual, information-rich resonance valleys through an asymmetric metasurface. By extracting multi-dip amplitude and phase-derivative features, MetaTap achieves ppb-level detection, representing a three orders of magnitude sensitivity leap over existing wireless methodologies.

10 CONCLUSION

In this paper, we present MetaTap, a passive metasurface-based system for high-resolution water contaminant sensing. MetaTap moves beyond conventional frequency-shift-based sensing by introducing a robust amplitude-phase spectral analysis, together with a novel Complementary Asymmetric Split Square (CASS) metasurface design that enables multi-dip feature encoding within a limited bandwidth. The derivative features of both amplitude and phase effectively mitigate multipath effects and substantially improve system robustness across complex, real-world scenarios. Guided by a physically interpretable model, MetaTap achieves an average prediction accuracy of 94.6% across multiple contaminants in real tap water, while effectively adapting to unmodeled environmental variations. With a fabrication cost of only $0.10 per metasurface, MetaTap provides a scalable and practical pathway for large-scale water quality monitoring, especially in underserved regions where access to safe drinking water remains a critical challenge.

References

[1] 2025. CST Studio Suite. https://www.3ds.com/products/simulia/cst-studio-suite

[2] United States Environmental Protection Agency. 2024. Basic Information about Lead in Drinking Water. https://www.epa.gov/ground-water-and-drinking-water/basic-information-about-lead-drinking-water

[3] Apple. 2025. Ultra Wideband information. https://support.apple.com/guide/iphone/ultra-wideband-information-iph771fd0aad/ios

[4] Juan Domingo Baena, Jordi Bonache, Ferran Martín, R Marqués Sillero, Francisco Falcone, Txema Lopetegi, Miguel AG Laso, Joan Garcia-Garcia, Ignacio Gil, M Flores Portillo, et al. 2005. Equivalent-circuit models for split-ring resonators and complementary split-ring resonators coupled to planar transmission lines. *IEEE transactions on microwave theory and techniques* 53, 4 (2005), 1451–1461.

[5] Bimedis.com [n. d.]. Spectrometer. https://bimedis.com/a-item/spectroscopy-equipment-bfrl-wqf-510-1946874

[6] Blender. 2025. Blender 4.4. https://www.blender.org/

[7] JS Bobowski. 2013. Using split-ring resonators to measure the electromagnetic properties of materials: An experiment for senior physics undergraduates. *American Journal of Physics* 81, 12 (2013), 899–906.

[8] Brazil (AP) BRASILIA. 2025. In Brazil, mining giant Vale is sued over metal contamination found in Indigenous peoples. https://apnews.com/article/brazil-indigenous-amazon-mining-cop30-vale-xikrin-9f8643135fad5fbcfe6092b1dec00304

[9] A Catenaccio, Y Daruich, and C Magallanes. 2003. Temperature dependence of the permittivity of water. *Chemical physics letters* 367, 5-6 (2003), 669–671.

[10] Baicheng Chen, John Nolan, and Xinyu Zhang. 2024. MetaBioLiq: A Wearable Passive Metasurface Aided mmWave Sensing Platform for BioFluids. In *Proceedings of the 30th Annual International Conference on Mobile Computing and Networking*. 1192–1206.

[11] Mohammad Cheraghinia, Adnan Shahid, Stijn Luchie, Gert-Jan Gordebeke, Olivier Caytan, Jaron Fontaine, Ben Van Herbruggen, Sam Lemey, and Eli De Poorter. 2024. A comprehensive overview on uwb radar: Applications, standards, signal processing techniques, datasets, radio chips, trends and future research directions. *IEEE Communications Surveys & Tutorials* (2024).

[12] Kenneth S Cole and Robert H Cole. 1941. Dispersion and absorption in dielectrics I. Alternating current characteristics. *The Journal of chemical physics* 9, 4 (1941), 341–351.

[13] Longqing Cong, Manukumara Manjappa, Ningning Xu, Ibraheem Al-Naib, Weili Zhang, and Ranjan Singh. 2015. Fano resonances in terahertz metasurfaces: a figure of merit optimization. *Advanced Optical Materials* 3, 11 (2015), 1537–1543.

[14] Natural Resources Defense Council. 2024. Flint Water Crisis: Everything You Need to Know. https://www.nrdc.org/stories/flint-water-crisis-everything-you-need-know

[15] Zhi-Min Dang, Jin-Kai Yuan, Sheng-Hong Yao, and Rui-Jin Liao. 2013. Flexible nanodielectric materials with high permittivity for power energy storage. *Advanced Materials* 25, 44 (2013), 6334–6365.

[16] Roy De Maesschalck, Delphine Jouan-Rimbaud, and Désiré L Massart. 2000. The mahalanobis distance. *Chemometrics and intelligent laboratory systems* 50, 1 (2000), 1–18.

[17] Ashutosh Dhekne, Mahanth Gowda, Yixuan Zhao, Haitham Hassanieh, and Romit Roy Choudhury. 2018. Liquid: A wireless liquid identifier. In *Proceedings of the 16th annual international conference on mobile systems, applications, and services*. 442–454.

[18] Centers for Disease Control and Prevention. 2025. Chemicals That Can Contaminate Tap Water. https://www.cdc.gov/drinking-water/causes/chemicals-that-can-contaminate-tap-water.html

[19] Lamia Goual. 2009. Impedance spectroscopy of petroleum fluids at low frequency. *Energy & Fuels* 23, 4 (2009), 2090–2094.

[20] Unsoo Ha, Junshan Leng, Alaa Khaddaj, and Fadel Adib. 2020. Food and liquid sensing in practical environments using {RFIDs}. In *17th USENIX symposium on networked systems design and implementation (NSDI 20)*. 1083–1100.

[21] Harold Hotelling et al. 1931. The generalization of Student's ratio. (1931).

[22] Yongzhi Huang, Kaixin Chen, Yandao Huang, Lu Wang, and Kaishun Wu. 2021. Vi-liquid: unknown liquid identification with your smartphone vibration. In *Proceedings of the 27th Annual International Conference on Mobile Computing and Networking*. 174–187.

[23] Wenli Jiao, Ju Wang, Yelu He, Xiangdong Xi, and Fuwei Wang. 2023. SoilTAG: fine-grained soil moisture sensing through chipless tags. *IEEE Transactions on Mobile Computing* 23, 3 (2023), 2153–2170.

[24] Wenli Jiao, Ju Wang, Yelu He, Xiangdong Xi, Fuwei Wang, Dingyi Fang, and Xiaojiang Chen. 2023. Eliminating design effort: A reconfigurable sensing framework for chipless, backscatter tags. *IEEE/ACM Transactions on Networking* 32, 2 (2023), 1155–1170.

[25] Abolghasem Jouyban, Shahla Soltanpour, and Hak-Kim Chan. 2004. A simple relationship between dielectric constant of mixed solvents with solvent composition and temperature. *International journal of pharmaceutics* 269, 2 (2004), 353–360.

[26] V Komarov, S Wang, and J Tang. 2005. Permittivity and measurements. (2005).

[27] Alexandros Ch Lazanas and Mamas I Prodromidis. 2023. Electrochemical impedance spectroscopy a tutorial. *ACS measurement science au* 3, 3 (2023), 162–193.

[28] Xiuqiang Li and Hui Ying Yang. 2021. A global challenge: clean drinking water. *Global Challenges* 5, 1 (2021).

[29] Yumeng Liang, Anfu Zhou, Huanhuan Zhang, Xinzhe Wen, and Huadong Ma. 2021. Fg-liquid: A contact-less fine-grained liquid identifier by pushing the limits of millimeter-wave sensing. *Proceedings of the ACM on Interactive, Mobile, Wearable and Ubiquitous Technologies* 5, 3 (2021), 1–27.

[30] Yan Lu, Peng-Yuan Liu, Peng Xiao, and Hong-Wen Deng. 2005. Hotelling's T 2 multivariate profiling for detecting differential expression in microarrays. *Bioinformatics* 21, 14 (2005), 3105–3113.
[31] Lars Lundheim. 2002. On Shannon and" Shannon's Formula". *Telektronikk* 98, 1 (2002), 20–29.
[32] PQ Mantas. 1999. Dielectric response of materials: extension to the Debye model. *Journal of the European Ceramic Society* 19, 12 (1999), 2079–2086.
[33] Ricardo Marqués, Francisco Mesa, Jesus Martel, and Francisco Medina. 2003. Comparative analysis of edge-and broadside-coupled split ring resonators for metamaterial design-theory and experiments. *IEEE Transactions on antennas and propagation* 51, 10 (2003), 2572–2581.
[34] NOVELDA. 2025. NOVELDA Ultra-wideband Impulse Radar Transceiver SoC. https://novelda.com/technology/datasheets/
[35] NXP. 2025. NXP: i.MX RT1060: Crossover MCU with Arm® Cortex®-M7. https://www.nxp.com/products/i.MX-RT1060
[36] World Health Organization et al. 2021. A global overview of national regulations and standards for drinking-water quality. (2021).
[37] QORVO. 2025. Qorvo® Delivers Ultra-Wideband in Google® Pixel 6 Pro. https://www.qorvo.com/newsroom/news/2021/qorvo-delivers-ultra-wideband-in-google-pixel-6-pro
[38] Cole RH and KS Cole. 1941. Dispersion and absorption in dielectrics. *J. Chem. Phys* 9 (1941), 341.
[39] Olivier Rioul and José Carlos Magossi. 2014. On Shannon's formula and Hartley's rule: Beyond the mathematical coincidence. *Entropy* 16, 9 (2014), 4892–4910.
[40] SAMMOBILE. 2025. Ultra Wideband information. https://www.sammobile.com/news/uwb-explained-galaxy-s21-plus-s21-ultra
[41] Linda Schweitzer and James Noblet. 2018. Water contamination and pollution. In *Green chemistry*. Elsevier, 261–290.
[42] SensorLogicInc. 2025. SLMX4 Data Sheet. https://github.com/SensorLogicInc/modules/blob/main/docs/SLMX4_Data_Sheet_2022.pdf
[43] Fei Shang, Panlong Yang, Dawei Yan, Sijia Zhang, and Xiang-Yang Li. 2024. LiquImager: Fine-grained Liquid Identification and Container Imaging System with COTS WiFi Devices. *Proceedings of the ACM on Interactive, Mobile, Wearable and Ubiquitous Technologies* 8, 1 (2024), 1–29.
[44] Fei Shang, Panlong Yang, Yubo Yan, and Xiang-Yang Li. 2022. LiqRay: non-invasive and fine-grained liquid recognition system. In *Proceedings of the 28th annual international conference on mobile computing and networking*. 296–309.
[45] Fei Shang, Panlong Yang, Yubo Yan, and Xiang-Yang Li. 2023. PackquID: In-packet liquid identification using RF signals. *Proceedings of the ACM on Interactive, Mobile, Wearable and Ubiquitous Technologies* 6, 4 (2023), 1–27.
[46] TESPERT Store. 2025. Water Testing Kits for Drinking Water: 125 Strips 16 in 1 Well and Drinking Water Test Kit, TESPERT Water Test Strips with Hardness, pH, Lead, Iron, Copper, Chlorine, and More. https://www.amazon.com/Water-Testing-Kits-Drinking-Hardness/dp/B0BG63JJ3T?th=1
[47] Philippe Tassin, Lei Zhang, Rongkuo Zhao, Aditya Jain, Thomas Koschny, and Costas M Soukoulis. 2012. Electromagnetically induced transparency and absorption in metamaterials: the radiating two-oscillator model and its experimental confirmation. *Physical review letters* 109, 18 (2012), 187401.
[48] James D Taylor. 2001. *Ultra-Wideband Radar Systems*. CRC press.
[49] MS Venkatesh and GSV Raghavan. 2005. An overview of dielectric properties measuring techniques. *Canadian biosystems engineering* 47, 7 (2005), 15–30.
[50] Vincent J Vitanza. 2024. Beyond the Tap: The Flint, Michigan Water Crisis as an Issue of Environmental Racism. (2024).
[51] Juexing Wang, Binbin Xie, Yimeng Liu, Minhao Cui, Xiao Zhang, Guangjing Wang, Ke Sun, Zhichao Cao, Huacheng Zeng, Qingxu Jin, et al. 2026. SoilNutri: A Passive Metasurface-based, Low-cost System for Soil Moisture and Nitrogen Monitoring. *Proceedings of the ACM on Interactive, Mobile, Wearable and Ubiquitous Technologies* 10, 1 (2026), 1–28.
[52] Ju Wang, Jie Xiong, Xiaojiang Chen, Hongbo Jiang, Rajesh Krishna Balan, and Dingyi Fang. 2017. TagScan: Simultaneous target imaging and material identification with commodity RFID devices. In *Proceedings of the 23rd Annual International Conference on Mobile Computing and Networking*. 288–300.
[53] Binbin Xie, Jie Xiong, Xiaojiang Chen, Eugene Chai, Liyao Li, Zhanyong Tang, and Dingyi Fang. 2019. Tagtag: material sensing with commodity rfid. In *Proceedings of the 17th conference on embedded networked sensor systems*. 338–350.
[54] Ziyang Zhang, Matteo Dainese, Lech Wosinski, and Min Qiu. 2008. Resonance-splitting and enhanced notch depth in SOI ring resonators with mutual mode coupling. *Optics express* 16, 7 (2008), 4621–4630.